Strain-induced two-dimensional relaxor ferroelectrics in Se-doped PbTe

Zhanpeng Gong,[1] Jefferson Zhe Liu,[2] Xiangdong Ding,[1] Jun Sun,[1] and Junkai Deng[1,*]
[1]*State Key Laboratory for Mechanical Behavior of Materials, Xi'an Jiaotong University, Xi'an 710049, China*
[2]*Department of Mechanical Engineering, The University of Melbourne, Parkville, VIC 3010, Australia*

(Received 19 December 2023; accepted 5 February 2024; published 26 February 2024)

Triggered by external fields, typical ferroelectrics (FEs) undergo a sharp phase transition from the nonpolarized paraelectric (PE) phase, which induces the emergence of spontaneous electric polarization. It is widely accepted that by introducing a large number of point defects, conventional FEs can be transformed into relaxor FEs, which exhibit unique physical properties, such as polar nanoregions (PNRs) and a corresponding gradual phase transition. In recent years, the discovery of two-dimensional (2D) FEs has attracted significant interest driven by the increasing demand for miniaturized nanoelectronics. Despite the identification of various 2D FE materials, there has been no report on 2D relaxor FEs so far. In this study, we explore the strain-induced FE phase transitions in a Se-doped PbTe monolayer through molecular dynamics simulations utilizing a developed deep-learning potential. Our findings reveal the gradual emergence of PNRs during the strain-induced FE phase transition of $Pb_{50}Te_{50-x}Se_x$ ($x \geqslant 4$). Additionally, we showcase the dynamic nature of the PNRs through a comparison between the instantaneous and time-averaged dynamic pair distribution functions. Furthermore, we demonstrate that the evolution of the PNRs' size and percolation strength with increasing strain can be well fitted by power laws derived from the percolation theory, which is a key characteristic of the relaxor-to-FE phase transition. Finally, a strain-temperature PE-relaxor-FE phase diagram for $Pb_{50}Te_{46}Se_4$ is presented, which provides valuable insights for potential applications involving 2D Se-doped PbTe.

DOI: 10.1103/PhysRevB.109.054117

I. INTRODUCTION

Conventional ferroelectric (FE) materials typically undergo an abrupt phase transition from a nonpolar to a polar state when subjected to temperature or an electric field, which is important for numerous applications [1]. By incorporating a large amount of additional elemental impurities as point defects (such as doping $PbNbO_3$ with Mg), conventional FEs can be transformed into a glassy polar state characterized by a diffuse phase transition and nanosized polar regions; these materials are named relaxor FEs or more simply relaxors [2]. Relaxor FEs are regarded as a more disordered and complex form of FE materials due to the incorporated impurities [2,3]. The consequent breaking of the long-range crystal order, combined with the emergence of random polar nanoregions (PNRs), leads to some unique physical properties, including a gradual phase transition and the lack of a clear hysteresis [4]. The disordered nature of relaxor FEs offers advantages in specific applications that require a broader operating temperature range, high sensitivity, and exceptional electromechanical response [3,4].

With the miniaturization of FE devices, nanoscale FE materials are becoming increasingly desirable. Among these, two-dimensional (2D) FEs hold significant promise for the next generation of nanoelectronics due to their atomic thickness [5–7]. Theoretical and experimental studies have proposed numerous 2D FEs, including transition-metal dichalcogenides (such as d1T-$MoTe_2$ [8] and WTe_2 [9]), group-IV metal chalcogenides (such as $CuInP_2S_6$) [10], and the group-IV chalcogenide 2D materials *MX*s (M = Ge, Sn; X = S, Se, Te) [11–13]. Recently, lead chalcogenide Pb*X* (X = S, Se, or Te) monolayers, which are intrinsically non-FE materials, have been reported to possess robust ferroelectricity when subjected to an adequate in-plane strain [14]. This discovery has introduced a potential category of valuable room-temperature 2D FEs. Despite the discovery of various 2D FE materials, there has been no report on 2D relaxor FEs to date. Therefore, it is highly desirable to explore 2D relaxor FEs, which could provide a unique platform for investigating their physical differences with respect to 2D FEs.

In this study, we developed a deep potential (DP) model to investigate the phase transition of Se-doped PbTe. The accuracy of the trained DP model was validated by successfully reproducing the density functional theory (DFT) predictions across a larger configurational space. By performing molecular dynamics (MD) simulations with the verified DP potential, we demonstrated the transformation of 2D PbTe from an FE state to a relaxor state through the incorporation of Se atoms. Notably, Se-doped PbTe exhibited a diffuse phase transition induced by an applied strain, which is in contrast with the abrupt phase transition observed for pristine FE PbTe. Additionally, we unveiled the dynamic-dependent nature of $Pb_{50}Te_{50-x}Se_x$ by identifying differences between the instantaneous and time-averaged structures, which only emerge in Se-doped samples. Further analysis revealed the continuous evolution of the PNRs during the phase transition, with the fastest increase in cluster size and percolation strength

*Corresponding author: junkai.deng@mail.xjtu.edu.cn

occurring near the strain at which the piezoelectric coefficients are maximum. These relationships conform to power laws in the percolation theory, which is a key characteristic of the relaxor-to-FE phase transition. Finally, a strain-temperature paraelectric (PE) -relaxor-FE phase diagram was established for $Pb_{50}Te_{46}Se_4$ and compared with that of PbTe. It is envisaged that these results will guide applications based on the strain-induced relaxor behavior of 2D Se-doped PbTe materials.

II. COMPUTATIONAL METHODS

A. Machine-learning interatomic potential (DP model)

The DEEPMD-kit package [15] is capable of constructing deep-learning based representations of potential energy surfaces to perform MD simulations. Compared to classic force fields, which are typically based on analytically formulated functionals, the DP model employing symmetry-preserving descriptors and dynamical embedding of the configurations into descriptors demonstrates a significantly higher level of accuracy [16,17]. This package has a broad range of potential applications, from finite molecules to extended systems and from metallic systems to chemically bonded systems [18].

In the DP model, the potential energy E of an atomic configuration is represented as the sum of the atomic energy E_i of each atom i, which is obtained from the descriptors through a fitting network. These descriptors characterize the local environment of atom i within a cutoff radius R_c of 7.5 Å. The maximum number of allowable atoms within this R_c is 95 for Pb, Te, and Se. To preserve the translational, rotational, and permutational symmetries of the descriptors, an embedding network is used. In addition, a smooth edition of the DP model is employed to remove the discontinuity introduced by the cutoff radius, with the inner cutoff set to 7.2 Å. The sizes of the embedding and fitting networks are (25, 50, 100) and (240, 240, 240), respectively. The loss function is defined as

$$L(p_\varepsilon, p_f, p_\xi) = p_\varepsilon \Delta\epsilon^2 + \frac{p_f}{3N}\sum_i |\Delta \boldsymbol{F}_i|^2 + \frac{p_\xi}{9}\|\Delta\xi\|^2, \quad (1)$$

where $\Delta\epsilon$, $\Delta \boldsymbol{F}_i$, and $\Delta\xi$ represent the differences in the energy, force, and virial tensor between the predictions of the DP model and the DFT data. p_ε, p_f, and p_ξ are the weight coefficients of the energy, force, and virial tensor, respectively. During the training procedure, p_ε increases from 0.02 to 1, while p_f decreases from 1000 to 1. In this study, $p_\xi = 0$ as the virial tensor was not used.

B. Generation of the training dataset and exploration protocol

In the current study, to cover the relevant phase space efficiently, we employed the DP generator (DP-GEN) [19] to produce the configurations for training the DP model. DP-GEN adopts a concurrent learning procedure that involves training, exploration, and labeling, as well as the iteration of the above steps until the required accuracy is obtained.

To perform the concurrent learning procedure, an initial dataset including 500 randomly distributed configurations was generated using the *ab initio* molecular dynamics (AIMD) method. The projector augmented-wave method [20,21] was used to treat the core and valence electrons, and the generalized gradient approximation of the Perdew, Burke, and Ernzerhof functional was adopted to account for the electron exchange-correlation interaction [22]. To ensure the accuracy of the results, an energy cutoff of 500 eV, a Gaussian smearing of 0.05 eV, and a k-point meshing of $5 \times 5 \times 1$ were used for all the calculations. A 20- Å-thick vacuum layer was added to a 36-atom slab to avoid the interaction of the neighbor monolayer $Pb_{50}Te_{50-x}Se_x$, which represents the 2D system. These settings were verified to be suitable for studying the 2D PbTe system by previous works [14,23]. The initial atomic structures for the AIMD simulations contained the ground state (space group *Cmcm*) and the strained conditions. Additionally, the occupancy and content of the Se atoms were varied ($Pb_{50}Te_{50-x}Se_x$, with x in the range of 0–20). Finally, the initial dataset was made up of the fully relaxed AIMD trajectories sampled from an *NVT* ensemble.

Based on the initial dataset, four DP models were trained with different initializations of the neural networks. One of the models was used to perform MD/MC (Monte Carlo) simulations for different strain conditions and Se concentrations at the temperature range of 10–400 K, exploring the relevant phase space. For all the other models, the energies and atomic forces of the produced MD trajectories were predicted. Furthermore, the maximum deviation of the four DP model predictions for the forces ($\sigma_f^{\max}$) provided a criterion for conducting the labeling:

$$\sigma_f^{\max} = \max_i \sqrt{\langle |\boldsymbol{F}_i - \langle \boldsymbol{F}_i \rangle|^2 \rangle}, \quad (2)$$

where $\boldsymbol{F}_i$ is the atomic force of the given configuration, and $\langle |\boldsymbol{F}_i - \langle \boldsymbol{F}_i \rangle|^2 \rangle$ represents the average over the four models. Reasonable upper (σ_{high}) and lower (σ_{low}) bounds for $\sigma_f^{\max}$ are 0.05 and 0.20 eV/Å [19,24], respectively. The configurations where $\sigma_f^{\max}$ was higher than σ_{high} usually exhibited highly distorted and unphysical features. On the other hand, we deemed that accurate predictions had been made for the configurations where $\sigma_f^{\max}$ was lower than σ_{low}. Thus, we labeled the configurations where $\sigma_f^{\max}$ lies between σ_{high} and σ_{low} to enable a wider vision of the DP model. The whole DP-GEN workflow stopped when the $\sigma_f^{\max}$ of 99% of the configurations was lower than σ_{low}. Finally, about 35 000 configurations were labeled and provided our training dataset.

C. MD simulations of the phase transition

Using the converged DP model, equilibrium MD simulations were carried out with periodic boundary conditions using the LAMMPS software package [25] within the temperature range of 10–400 K. As for the DFT set, a vacuum layer with a thickness of at least 20 Å was added to the monolayer $Pb_{50}Te_{50-x}Se_x$ in all MD simulations. To eliminate the possible influence of the size, a sufficiently large supercell ($60 \times 60 \times 1$ with 14 400 atoms) was used to obtain the converged results. The phase-space trajectory was determined using the velocity Verlet algorithm with a time step of 1 fs. The temperature and pressure were controlled using the Nosé-Hoover thermostat and the Parrinello-Rahman barostat, respectively [26,27]. The so-called quasistatic loading procedure was employed with a strain interval of 0.1% (engineering strain) [28]. To obtain reliable information on

the phase transition, at each loading, the total energies of the systems were firstly converged in the equilibrium run of 10 ps, and the configurations used for the analysis were subsequently sampled in the production run of 30 ps. The distributions of the Se atoms were optimized via MC calculations after every 1% strain loading with 50 000 steps. Additionally, three initial atomic configurations with different Se distributions were set up to eliminate the randomness of the results. Notably, the results of these three calculations were identical.

For a better investigation of the phase transition, the local polarization (P) was calculated and monitored during strain loading. P can be easily obtained by multiplying the Born effective charges (Z_i^*) with their displacement ($\boldsymbol{u}_i$) concerning the equilibrium structure (undistorted PE PbTe):

$$P = \sum_{\text{unit cell}} Z_i^* \boldsymbol{u}_i / S_{\text{cell}}. \tag{3}$$

For the 2D scenario, we employed the in-plane area of the unit cell (S_{cell}) instead of volume to define the dipole density. The atomic positions were collected every 1 ps for calculating the charge displacements ($\boldsymbol{u}_i$). The Born effective charge tensors in the uniaxially strained cases of PbTe and PbSe were diagonalized in our DFT calculations. Therefore, vectors instead of tensors were used to calculate the polarization, and these vectors were $\langle 3.94\,890, 4.37\,462, 0.29\,075\rangle$, $\langle -3.94\,889, -4.37\,461, -0.29\,076\rangle$, and $\langle -3.61903, -3.75568, -0.37324\rangle$ for the Pb, Te, and Se atoms in the X, Y, and Z directions, respectively, of the $b(Y)$ strained case. For simplicity, we did not take into account the variations in the Born effective charges due to the change in the chemical environment, which would require an upgrade of the methodology [29,30]. We used the dynamic pair distribution function (DPDF) method [31,32] to characterize the structure changes during the phase transition. Based on the MD trajectories, we calculated the instantaneous DPDF [$g(r,t)$], which represents the probability to find a pair of atoms at a distance r with a time delay t:

$$g(r,t) = q \sum_{i,j=1}^{N} \frac{1}{4\pi r^2} \int e^{-[(r-|\boldsymbol{R}_i(t')-\boldsymbol{R}_j(t+t')|)^2/s]} dt', \tag{4}$$

where q and s are the normalization factors, N is the number of atoms, and $\boldsymbol{R}$ is the atomic position. $g(r,t)$ can be Fourier transformed to $G(r,\omega)$, which denotes the DPDF. More details regarding the DPDF method can be found in the literature [33,34].

III. RESULTS AND DISCUSSION

A. Verification of the DP model

We evaluated the predictive capability of our DP model on the validation dataset sampled from the short MD run in the DP-GEN procedure. This dataset consists of 3000 frames, each accompanied by self-consistent DFT calculations. The comparison between the results of the DFT and DP model regarding energies and atomic forces is provided in Fig. 1. The content of Se atoms ranges from 0% to 12% in differently strained configurations, and the temperature spans from 10 to 400 K for the validation dataset. These results reveal a consistent agreement between the DFT calculations and the

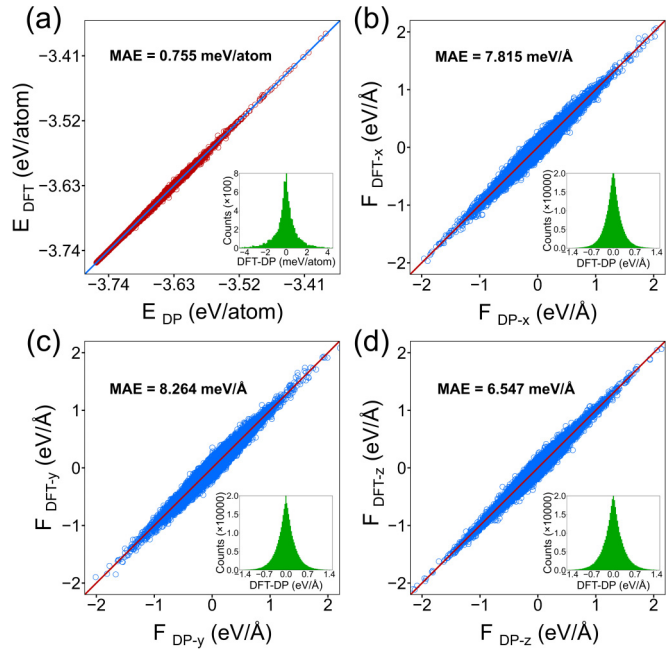

FIG. 1. Comparisons of the energies and forces between the DFT and DP model for the variously strained structures sampled from the temperature range of 10–400 K with different Se contents. Energies per atom (a) and atomic forces [(b), (c), and (d) for the pseudo x, y, and z directions, respectively] of the structures which are not included in the training dataset. The insets show the distributions of the absolute errors, and the lines show the perfect correlations of the corresponding variables.

DP model predictions across a broad configurational space, with mean absolute errors of 0.755 meV/atom for the energy and 7.815, 8.264, and 6.547 meV/Å for the forces in the X, Y, and Z directions, respectively. These findings demonstrate that the proposed DP model is sufficiently accurate [28,35].

We further validated the accuracy of our DP model across various configurations of the Se-doped PbTe using the MC calculation. The Se atoms were redistributed through DFT-based MC calculations to achieve a more stable configuration of the $Pb_{50}Te_{50-x}Se_x$ system. The energy profiles obtained from the DFT and DP model during the MC calculations for $Pb_{50}Te_{46}Se_4$ ($6 \times 6 \times 1$ supercell, 144 atoms) in both the PE and the strained states are depicted in Fig. 2. The

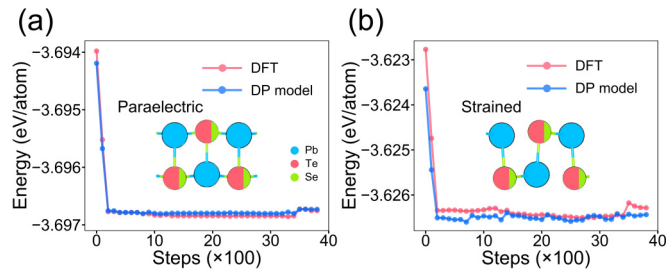

FIG. 2. Comparisons of the energies between the DFT and DP model for different atomic configurations during the MC process of $Pb_{50}Te_{46}Se_4$ in the (a) PE and (b) strained states. The insets show the representative structures.

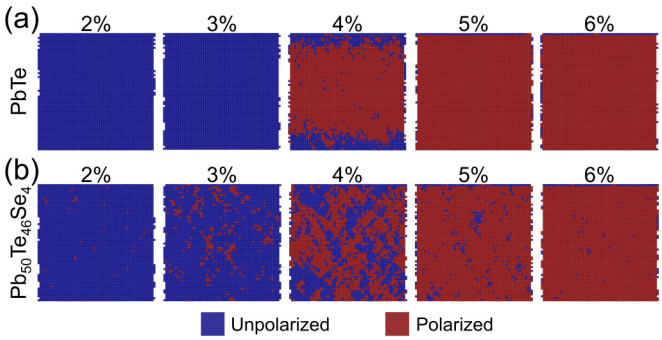

FIG. 3. Local distributions of the FE phase in pristine and Se-doped PbTe. (a) PbTe at a strain of 2%, 3%, 4%, 5%, and 6%. (b) $Pb_{50}Te_{46}Se_4$ at a strain of 2%, 3%, 4%, 5%, and 6%. The red color represents the FE phase, and the blue color indicates the PE phase.

supercells with the initial configurations are presented in Fig. S1 of the Supplemental Material [36]. The results indicate that the DP model precisely reproduces the energy profiles, which is critical for MD simulations of chemically disordered materials [37,38]. Furthermore, these results demonstrate that our developed DP model can faithfully reproduce the DFT energies over the large phase space of Se-doped PbTe with the different strain conditions and Se distributions, providing a valuable chance to yield atomic insights on the strain-induced phase transition process of $PbTe_{1-x}Se_x$ system in the larger temporal and spatial scale with DFT-level accuracy.

B. Strain-induced phase transition

To explore the strain-induced FE phase transition, we carried out MD simulations for both the pristine 2D PbTe and the Se-doped PbTe ($Pb_{50}Te_{46}Se_4$) alloys. Figure 3 shows the local polarization distribution for PbTe and $Pb_{50}Te_{46}Se_4$ during strain loading. It is noted that due to the second-order nature of the strain-indued FE phase transition of pristine 2D PbTe [14], the FE phase emerges at an applied strain of 4% [Fig. 3(a)], indicating the occurrence of an abrupt FE phase transition [14,39]. Conversely, in $Pb_{50}Te_{46}Se_4$, a smeared distribution of the polar clusters (marked in red) is observed for a strain ranging from 2% to 5%, as illustrated in Fig. 3(b). This indicates that nanosized polar clusters emerge diffusively, which suggests a frustration of the ferroelectric phase transition due to the existence of Se atoms. For comparison, Fig. S2 presents the results for the $Pb_{50}Te_{38}Se_{12}$ case (higher Se doping), which exhibits a similar behavior. Compared with the case with a lower Se concentration (4%), a higher Se concentration (12%) leads to larger cluster sizes for a specific strain. These observations coincide with the PNRs model widely used to explain the behaviors of classic bulk relaxors [40,41]. Thus, the present results demonstrate that FE 2D PbTe can be engineered into a 2D relaxor through the incorporation of Se atoms.

To depict the structural changes during strain loading, we utilized the instantaneous DPDF $g(r, t = 0)$ and the time-averaged DPDF $G(r, \omega = 0)$, as illustrated in Fig. 4. The most critical features of the DPDFs are the peak splitting at an

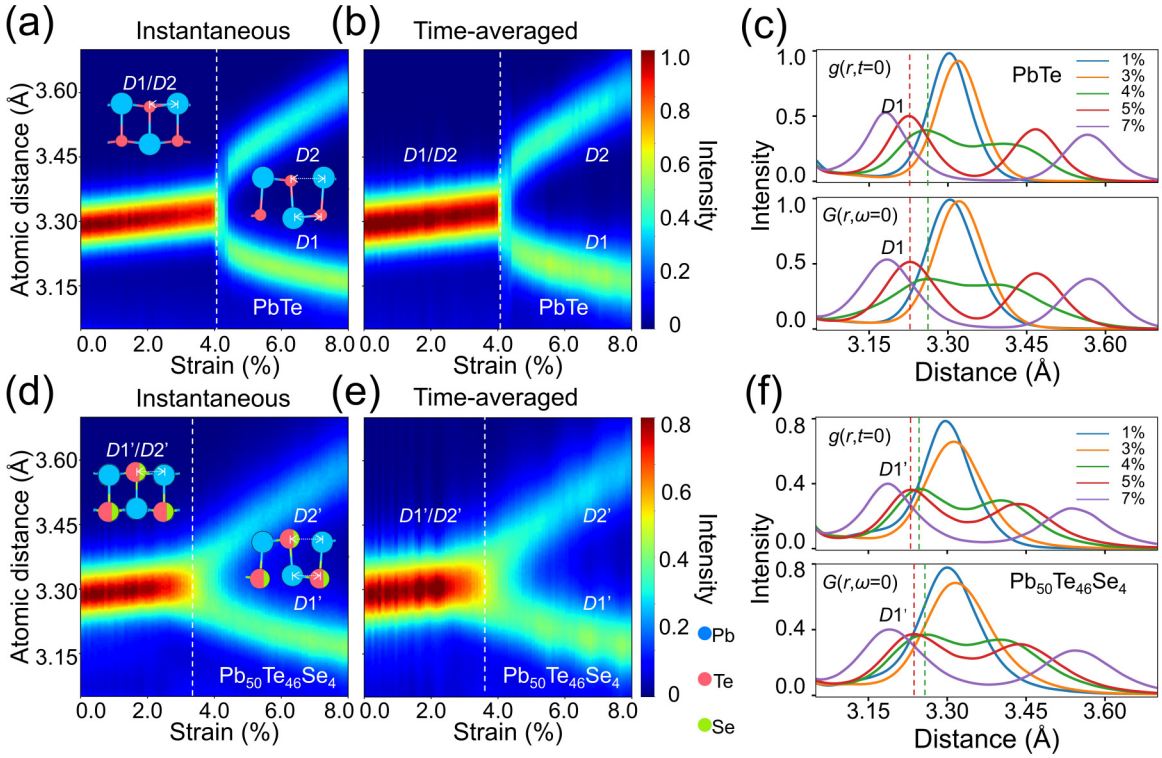

FIG. 4. DPDF profiles of pristine and Se-doped PbTe. Instantaneous DPDF of (a) PbTe and (d) $Pb_{50}Te_{46}Se_4$. Time-averaged DPDF of (b) PbTe and (e) $Pb_{50}Te_{46}Se_4$. 1D DPDF curves of (c) PbTe and (f) $Pb_{50}Te_{46}Se_4$. The inserted lines in (a), (b), (d), and (e) show the strain at which peak splitting starts. The inserted lines in (c) and (f) show the positions of the peaks with the corresponding color. The insets show the material structures in the PE and FE states of PbTe and $Pb_{50}Te_{46}Se_4$. The labels "*D*1" and "*D*2" indicate the corresponding DPDF peaks.

atomic distance of about 3.30 Å when loading with strains of 3%–5% for both the pristine PbTe [Figs. 4(a) and 4(b)] and $Pb_{50}Te_{46}Se_4$ [Figs. 4(d) and 4(e)] systems. Combined with previous studies [23,42], these peaks correspond to in-plane Pb-Te (Se) atomic distances. The observed peak splitting is ascribed to the in-plane reverse displacements of the Pb and Te (Se) atoms, indicating bond breaking.

For the pristine PbTe, peak splitting occurs at a strain of 4%, indicating the occurrence of the PE-to-FE phase transition, as shown in Fig. 4(a). In addition, the intensity distributions in Figs. 4(a) and 4(b) show no differences between the $g(r, t = 0)$ and $G(r, \omega = 0)$ cases, demonstrating the dynamic-independent nature of the abrupt phase transition. This is further highlighted in the one-dimensional (1D) DPDF curves in Fig. 4(c), where the peak positions, marked by the dashed lines of the same color [$D1$ corresponds to the shorter in-plane Pb-Te (Se) bonding], coincide for the $g(r, t = 0)$ and $G(r, \omega = 0)$ cases. By contrast, for $Pb_{50}Te_{46}Se_4$, Fig. 4(d) shows that the instantaneous peak splitting occurs at a strain of 3.3%, but Fig. 4(e) reveals that the time-averaged peak splitting takes place at a strain of 3.7%, both values being smaller than that of pristine PbTe. Figures S3(a) and S3(b) show similar behavior for Se-doped PbTe with a higher Se concentration (namely, $Pb_{50}Te_{38}Se_{12}$), indicating a further decrease in the strains at which a pronounced structure change occurred, i.e., 2.8% for $g(r, t = 0)$ and 3.1% for $G(r, \omega = 0)$, respectively. It is worth noting that the points at which peak splitting starts to occur are substantially different for the $g(r, t = 0)$ and $G(r, \omega = 0)$ in both $Pb_{50}Te_{46}Se_4$ and $Pb_{50}Te_{38}Se_{12}$ cases. Such differences in the strains at which peak splitting takes place for the $g(r, t = 0)$ and $G(r, \omega = 0)$ demonstrate the dynamic-dependent nature of the relaxor state in $Pb_{50}Te_{50-x}Se_x$, which is due to the existence of dynamic PNRs with various sizes.

In addition, the comparison between Figs. 4(a) and 4(d) reveals that the incorporation of Se atoms induces a change in the character of the phase transition. This is evident in the shift from an abrupt phase transition, marked by a sharp peak splitting, to a more gradual phase transition characterized by continuous peak splitting. Such a transformation is further elucidated in Fig. S4, where the intensity changes occurring at an atomic distance of 3.32 Å for both pristine PbTe and $Pb_{50}Te_{46}Se_4$ during strain loading are presented. In the case of pristine PbTe, a sharp drop in intensity is observed at a strain of 4%. Conversely, $Pb_{50}Te_{46}Se_4$ exhibits a gradual intensity decrease starting at a strain of 1.9%, which is in agreement with the results presented in Fig. 3(b) regarding the emergence of PNRs. These phenomena are similar to the behaviors observed in perovskite relaxor FEs and strain glasses [32,43].

Furthermore, we present the change in the peak positions, which corresponds to the change in the atomic distance between Pb and Te (Se), in the 1D DPDF curves at different strains in Fig. 5. The curves for pristine PbTe and $Pb_{50}Te_{46}Se_4$ were extracted from the contour plots at various strains for the $g(r, t = 0)$ and $G(r, \omega = 0)$ cases. The instantaneous (D_{inst}) and time-averaged (D_{avg}) peak position changes in Figs. 5(a) and 5(b) are defined as the absolute differences of the peak positions from the baseline of the average in-plane Pb-Te (Se) distance in the 4% strained state, i.e., 3.32 Å in the current

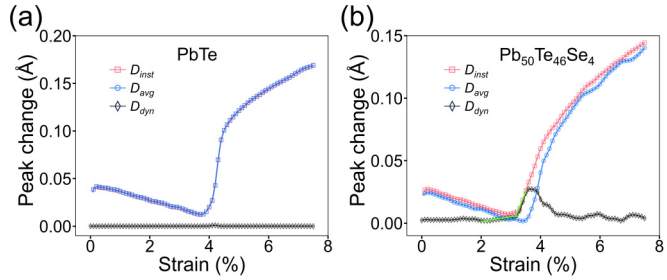

FIG. 5. Peak position change as a function of the applied strain for pristine PbTe and Se-doped PbTe. Instantaneous and time-averaged peak position changes and corresponding dynamic component of the peak position changes for (a) pristine PbTe and (b) $Pb_{50}Te_{46}Se_4$. The inserted lines are guides for the eye.

study. The peak position used after peak splitting is the smaller of the two peaks ($D1$). In addition, the dynamic component (D_{dyn}) of the peak position change is defined as the difference between D_{inst} and D_{avg}; such a component serves as an indicator of the dynamic-dependent behavior.

For the pristine PbTe, as shown in Fig. 5(a), both D_{inst} and D_{avg} increase simultaneously, indicating that there is no delay of D_{avg} during strain loading. Additionally, when considering Fig. 3(a), where a synchronous emergence of polarization occurs in the whole system at a critical strain due to the second-order nature of the phase transition, it can be concluded that this behavior is caused by the absence of dynamic PNRs in pristine 2D PbTe [41]. By contrast, the results for $Pb_{50}Te_{46}Se_4$ are notably different from the pristine case. Figure 5(b) reveals that D_{inst} and D_{avg} are coincident before the strain reaches 1.9%, resulting in a zero D_{dyn}. However, as indicated by the inserted lines in Fig. 5(b), when the strain exceeds this value, D_{inst} starts to increase while D_{avg} remains unchanged, yielding nonzero D_{dyn} values. Additionally, the maximum of D_{dyn} (3.5%) occurs at a strain value between the strains at which peak splitting takes place in Figs. 4(d) and 4(e). These phenomena are attributed to the emergence of dynamic PNRs [41], resembling the behavior observed in classic relaxor FEs and strain glasses [32,43]. Furthermore, for strains larger than 5.7%, D_{inst} and D_{avg} converge again and reach a considerable magnitude, suggesting that the whole system is in the FE state, which is in agreement with our observations in Fig. 3(b). A similar process occurs for the $Pb_{50}Te_{38}Se_{12}$ case (Figs. S2 and S5) with a lower triggering strain. Hence, unlike for pristine PbTe, the transition between the PE and FE states is interrupted by an intermediate dynamic PNRs-induced relaxor state for Se-doped PbTe.

C. Percolation effects of 2D relaxor FE

To make a further comparison of the PE-to-FE phase transition between pristine PbTe and $Pb_{50}Te_{50-x}Se_x$, we investigated the evolution of the polarization, PNRs size, and percolation effect of the PNRs during strain loading. The average polarizations and corresponding piezoelectric coefficients (d_{11}) with applied strain for pristine PbTe and $Pb_{50}Te_{46}Se_4$ are presented in Figs. 6(a) and 6(b), respectively. It is observed that the average polarization of pristine PbTe increases more rapidly at the transition strain of 4% [Fig. 6(a)] compared with

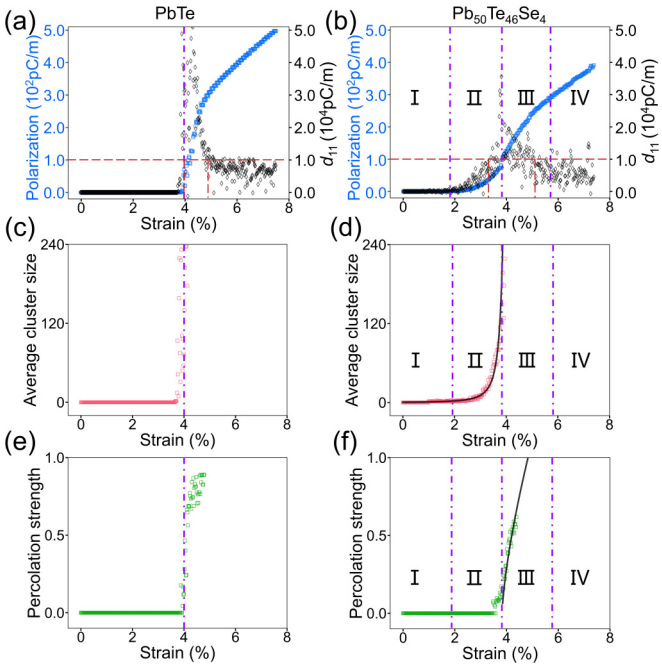

FIG. 6. Evolutions of polarization and polarized clusters with strain for pristine and Se-doped PbTe. Average polarization, piezoelectric coefficient (d_{11}), average size of the polarized clusters, and percolation strength of pristine PbTe [(a), (c), and (e), respectively] and $Pb_{50}Te_{46}Se_4$ [(b), (d), and (f), respectively]. The black lines are the fitting curves according to the percolation theory, while the other lines are guides for the eye.

that of $Pb_{50}Te_{46}Se_4$, for which the PNRs emerge at a strain of 1.9% [Fig. 6(b)]. This observation is consistent with the features observed in the phase transitions illustrated in Figs. 3 and 4 and Fig. S4. As a result, a considerable d_{11} (greater than the stable value of 0.7 pC/N) is found only within a narrow strain range (about 0.8%) near the strain of 4% for pristine PbTe. However, for the $Pb_{50}Te_{46}Se_4$ case, a large d_{11} is observed starting from a lower strain (3.3%) and within a broader strain range (about 2%), demonstrating an enhanced piezoelectric performance of PbTe during the PE-to-FE phase transition induced by Se doping. This is further supported by the case in which more Se was added (the $Pb_{50}Te_{38}Se_{12}$ case in Fig. S6), which exhibits a lower triggering strain (2.7%) and a much broader strain range (2.6%).

Moreover, according to Fig. 6(a), the phase transition of pristine PbTe is abrupt, with the nonpolarized PE state changing suddenly to a polarized FE state. By contrast, according to the d_{11} trend during strain loading, the phase transition process for $Pb_{50}Te_{50-x}Se_x$ can be divided into four stages, as illustrated in Fig. 6(b) and Fig. S6(a). The first stage corresponds to the elastic deformation of the PE state of $Pb_{50}Te_{50-x}Se_x$, where no polarization is observed. The second stage lies between the start of the nonzero d_{11} and its maximum, corresponding to the emergence of scattered PNRs. The third stage occurs between the peak of d_{11} and the beginning of its convergence to the stable value, suggesting the evolution of PNRs growth under strain loading. Finally, the fourth stage corresponds to the strain interval where d_{11} has converged to a steady value, indicating the FE state of $Pb_{50}Te_{50-x}Se_x$.

The different polarization change behaviors observed in pristine PbTe and $Pb_{50}Te_{46}Se_4$ can be attributed to the different evolution processes of the polarized clusters, as evidenced by Fig. 3. To elucidate the differences between the two cases, we defined two significant quantities based on the percolation theory [44], which has proven effective in analyzing the field-induced phase transition from the relaxor to the FE state [45]. One of these quantities is the average size of PNRs:

$$\langle s \rangle = \langle N^2 \rangle / \langle N \rangle, \tag{5}$$

where N is the number of unit cells in the PNRs, and $\langle \cdots \rangle$ denotes the average over all the PNRs belonging to the supercell. The other is the so-called strength of the percolated cluster, which is given by

$$P_\infty = N_\infty / N_{SC}, \tag{6}$$

where N_∞ is the number of unit cells belonging to the infinite percolating cluster, and N_{SC} is the number of unit cells in the supercell. The cluster is considered percolated when it extends from one side of the supercell to the opposite side along the [100] (x) or [010] (y) direction.

In pristine PbTe, due to the nature of the second-order phase transition, the average cluster size [Fig. 6(c)] and percolation strength [Fig. 6(e)] diverge at the critical strain (4%). This divergence corresponds to the point where the polarization and d_{11} exhibit a sharp increase due to the sudden emergence of the FE phase in the whole system, as shown in Fig. 3(a). On the contrary, $Pb_{50}Te_{46}Se_4$ displays noticeable differences. In stage I, both the average cluster size and the percolation strength remain zero, which represents a typical elastic behavior. Beyond the strain of 1.9% (stage II), the average cluster size begins to increase, as presented in Fig. 6(d), while the percolation strength remains zero, as illustrated in Fig. 6(f). This indicates the gradual growth of the PNRs before the infinite cluster emerges. Notably, the average cluster size undergoes a rapid increase as it approaches the inflection point of the average polarization curve. As the strain surpasses this point (stage III), the percolation strength experiences a dramatic increase, suggesting the onset of the percolation of the infinite cluster. In stage IV, through the merging of the PNRs to form the infinite cluster, the local unpolarized regions vanish, indicating the establishment of a complete FE state, as shown in Fig. 3(b). Interestingly, due to the swift transition of the unpolarized region into the polarized region during the percolation of the infinite cluster, the strain at which d_{11} is maximum coincides with the strain at which cluster percolation starts, namely, the inflection point of the average polarization curve [Figs. 6(b), 6(d), and 6(f)]. Similar behaviors were also observed for the system doped with 12% Se (Fig. S6) at a lower percolation strain (e_{inf_p}), i.e., 3.9% strain for $Pb_{50}Te_{46}Se_4$ and 3.4% strain for $Pb_{50}Te_{38}Se_{12}$.

Importantly, the relationship between the average PNRs size and strain can be well fitted by the power law $C/(e_{\mathrm{inf}\_p} - e)^{\gamma_e}$, as shown by the black curve in Fig. 6(d), which is widely adopted in the standard percolation theory

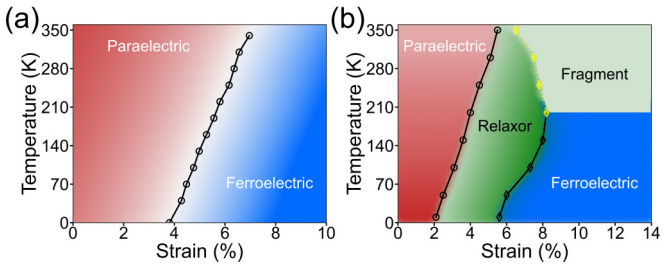

FIG. 7. Strain-temperature phase diagram of 2D (a) pristine PbTe [14] and (b) $Pb_{50}Te_{46}Se_4$ determined by MD simulations. The diagram for pristine PbTe is reprinted from Ref. [14]. The dashed line indicates the strain at which $Pb_{50}Te_{46}Se_4$ breaks down.

[44,45]. The calculated γ_e values are 2.3 and 2.5 for Se additions of 4% and 12% (Fig. S6), respectively. Additionally, the change in percolation strength with increasing strain can also be well fitted by the power law $(e - e_{\text{inf}\_p})^{\beta_e}$, as shown by the black curve in Fig. 6(f), which is another prominent feature in the standard percolation theory [44,45]. The β_e values are determined to be 0.7 for $Pb_{50}Te_{46}Se_4$ and 0.75 for $Pb_{50}Te_{38}Se_{12}$ (Fig. S6). Possibly due to the dimensionality and lattice-related factors [44], these values differ from the results obtained for the electric-field-induced macroscopic polarization transformation in bulk $Ba(Zr, Ti)O_3$ [45], which are 1.0–1.3 for γ_e and 0.6–0.7 for β_e. Notably, the rapid increase in the average PNRs size can lead to the formation of an infinite cluster, indicated by the sequential burst of cluster size and the percolation strength in the vicinity of e_{inf_p}, as shown in Figs. 6(d) and 6(f), respectively. These results suggest that the percolation of the PNRs in 2D $Pb_{50}Te_{46}Se_4$ takes place during the strain-induced relaxor-to-FE transition, with the strain playing a similar role to the composition change in the conventional percolation theory [44]. These power-law correlations are related to the physical characteristics of relaxors, which have been theoretically and experimentally demonstrated to follow the percolation of polarized clusters [45–47].

Finally, based on the polarization change and the corresponding change in d_{11} with increasing strain, we determined PE-to-FE phase diagrams for both pristine PbTe [14] and $Pb_{50}Te_{46}Se_4$ at different temperatures, as presented in Fig. 7. Figure 7(a) illustrates that PbTe undergoes a PE-to-FE phase transition at the critical strain, which increases with increasing temperature, as demonstrated by our previous work [14]. For $Pb_{50}Te_{46}Se_4$, we consider the strain at the emergence of the PNRs as the transition point for the PE-to-relaxor process. In the present study, when we refer to the emergence of the PNRs, we are indicating the point where the first-order derivative of the average polarization concerning the strain (piezoelectric coefficient) starts to increase. Meanwhile, the transition point of the relaxor-to-FE process refers to the strain where the d_{11} converges to a stable value. We also provide the evolutions of the ratio of the polarized unit cell (area) to the supercell (area) at 10 and 50 K in Fig. S7, showing the same ratio (very close to zero) at the PE-to-relaxor point for different temperatures. Unlike for PbTe, Fig. 7(b) illustrates that $Pb_{50}Te_{46}Se_4$ first transitions from the PE state to the relaxor state at smaller strains and then reaches the FE state at larger strains at a temperature lower than 200 K. Notably, the strains of PE-to-relaxor transition increase with increasing temperature, which is consistent with the trend reported for pristine PbTe [14]. However, when the temperature exceeds 200 K, $Pb_{50}Te_{46}Se_4$ breaks down before the relaxor-to-FE transition, resulting in four distinct regions in the corresponding phase diagram: PE, relaxor, FE, and fragment regions. To illustrate the effect of Se doping concentration, we present the transition points related to Se concentration at 10 K in Fig. S8. The critical strain for the PE-to-relaxor phase transition decreases with an increase in Se addition. Conversely, the critical strain for the relaxor-to-FE phase transition increases with higher Se addition, thereby extending the strain range of the relaxor ferroelectric state in Se-doped PbTe.

IV. CONCLUSIONS

In summary, the phase transition processes of PbTe and $Pb_{50}Te_{50-x}Se_x$ $(x \geqslant 4)$ during strain loading were investigated and compared using MD simulations based on a deep-learning force field (DP model). The accuracy and generalization performance of our DP potential were thoroughly verified. Through MD simulations, the diffuse nature of the strain-induced FE transition of $Pb_{50}Te_{50-x}Se_x$ $(x \geqslant 4)$ is observed, marked by the gradual emergence of PNRs. This behavior is in contrast with the abrupt phase transition observed in pristine PbTe. Moreover, instantaneous and time-averaged DPDFs were employed to characterize the structure changes and revealed that the dynamic nature of $Pb_{50}Te_{50-x}Se_x$ is caused by the presence of PNRs. Further analysis unveiled a significant increase in PNRs size and percolation strength for $Pb_{50}Te_{50-x}Se_x$ near a critical strain, which can be well fitted by the power laws used in the percolation theory, providing a key characteristic of the relaxor-to-FE phase transition. Interestingly, this critical strain coincides with the location of the largest piezoelectric coefficient (d_{11}). Finally, the strain-temperature PE-relaxor-FE phase diagram of $Pb_{50}Te_{46}Se_4$ was determined, offering guidance for device design based on the strain-induced relaxor behavior of 2D Se-doped PbTe.

ACKNOWLEDGMENTS

The authors gratefully acknowledge the support of NSFC (Grant No.11974269), the support of the Key Research and Development Program of Shaanxi (Grant No. 2023-YBGY-480), and the 111 Projects 2.0 (Grant No. BP0618008). J. Z. L. acknowledges the support from ARC Discovery Projects (Grant No. DP210103888) and HPC from National Computational Infrastructure from Australia. The authors also thank F. Yang and X. D. Zhang at the Network Information Center of Xi'an Jiaotong University for supporting the HPC platform. This work is also supported by the high-performance computing power and technical support provided by Xi'an Future Artificial Intelligence Computing Center.

[1] M. Wu, 100 years of ferroelectricity, Nat. Rev. Phys. **3**, 726 (2021).

[2] D. Wang, X. Ke, Y. Wang, J. Gao, Y. Wang, L. Zhang, S. Yang, and X. Ren, Phase diagram of polar states in doped ferroelectric systems, Phys. Rev. B **86**, 054120 (2012).

[3] R. A. Cowley, S. N. Gvasaliya, S. G. Lushnikov, B. Roessli, and G. M. Rotaru, Relaxing with relaxors: A review of relaxor ferroelectrics, Adv. Phys. **60**, 229 (2011).

[4] F. Li, S. Zhang, D. Damjanovic, L.-Q. Chen, and T. R. Shrout, Local structural heterogeneity and electromechanical responses of ferroelectrics: Learning from relaxor ferroelectrics, Adv. Funct. Mater. **28**, 1801504 (2018).

[5] M. Si, A. K. Saha, S. Gao, G. Qiu, J. Qin, Y. Duan, J. Jian, C. Niu, H. Wang, W. Wu *et al.*, A ferroelectric semiconductor field-effect transistor, Nat. Electron. **2**, 580 (2019).

[6] S. Kamaei, X. Liu, A. Saeidi, Y. Wei, C. Gastaldi, J. Brugger, and A. M. Ionescu, Ferroelectric gating of two-dimensional semiconductors for the integration of steep-slope logic and neuromorphic devices, Nat. Electron. **6**, 658 (2023).

[7] Y. Joo, E. Hwang, H. Hong, S. Cho, and H. Yang, Memory and synaptic devices based on emerging 2D ferroelectricity, Adv. Electron. Mater. **9**, 2300211 (2023).

[8] S. Yuan, X. Luo, H. L. Chan, C. Xiao, Y. Dai, M. Xie, and J. Hao, Room-temperature ferroelectricity in $MoTe_2$ down to the atomic monolayer limit, Nat. Commun. **10**, 1775 (2019).

[9] Z. Fei, W. Zhao, T. A. Palomaki, B. Sun, M. K. Miller, Z. Zhao, J. Yan, X. Xu, and D. H. Cobden, Ferroelectric switching of a two-dimensional metal, Nature (London) **560**, 336 (2018).

[10] F. Liu, L. You, K. L. Seyler, X. Li, P. Yu, J. Lin, X. Wang, J. Zhou, H. Wang, H. He *et al.*, Room-temperature ferroelectricity in $CuInP_2S_6$ ultrathin flakes, Nat. Commun. **7**, 12357 (2016).

[11] K. Chang, J. Liu, H. Lin, N. Wang, K. Zhao, A. Zhang, F. Jin, Y. Zhong, X. Hu, W. Duan *et al.*, Discovery of robust in-plane ferroelectricity in atomic-thick SnTe, Science **353**, 274 (2016).

[12] K. Chang, F. Küster, B. J. Miller, J.-R. Ji, J.-L. Zhang, P. Sessi, S. Barraza-Lopez, and S. S. P. Parkin, Microscopic manipulation of ferroelectric domains in SnSe monolayers at room temperature, Nano Lett. **20**, 6590 (2020).

[13] R. Fei, W. Kang, and L. Yang, Ferroelectricity and phase transitions in monolayer group-IV monochalcogenides, Phys. Rev. Lett. **117**, 097601 (2016).

[14] Z. Gong, J. Z. Liu, X. Ding, J. Sun, and J. Deng, Strain-aided room-temperature second-order ferroelectric phase transition in monolayer PbTe: Deep potential molecular dynamics simulations, Phys. Rev. B **108**, 134112 (2023).

[15] H. Wang, L. Zhang, J. Han, and W. E, DeePMD-kit: A deep learning package for many-body potential energy representation and molecular dynamics, Comput. Phys. Commun. **228**, 178 (2018).

[16] L. Zhang, J. Han, H. Wang, R. Car, and W. E, Deep potential molecular dynamics: A scalable model with the accuracy of quantum mechanics, Phys. Rev. Lett. **120**, 143001 (2018).

[17] L. Zhang, J. Han, H. Wang, W. A. Saidi, R. Car, and E. Weinan, End-to-end symmetry preserving inter-atomic potential energy model for finite and extended systems, in *Proceedings of the 32nd International Conference on Neural Information Processing Systems (NIPS'18)* (Curran Associates Inc., Red Hook, NY, 2018), pp. 4441–4451.

[18] T. Wen, L. Zhang, H. Wang, Weinan E, and D. J. Srolovitz, Deep potentials for materials science, Mater. Futures **1**, 022601 (2022).

[19] Y. Zhang, H. Wang, W. Chen, J. Zeng, L. Zhang, H. Wang, and W. E, DP-GEN: A concurrent learning platform for the generation of reliable deep learning based potential energy models, Comput. Phys. Commun. **253**, 107206 (2020).

[20] G. Kresse and D. Joubert, From ultrasoft pseudopotentials to the projector augmented-wave method, Phys. Rev. B **59**, 1758 (1999).

[21] P. E. Blöchl, Projector augmented-wave method, Phys. Rev. B **50**, 17953 (1994).

[22] J. P. Perdew, K. Burke, and M. Ernzerhof, Generalized gradient approximation made simple, Phys. Rev. Lett. **77**, 3865 (1996).

[23] B. Xu, Z. Gong, J. Liu, Y. Hong, Y. Yang, L. Li, Y. Liu, J. Deng, and J. Z. Liu, Tunable ferroelectric topological defects on 2D topological surfaces: Complex strain engineering skyrmion-like polar structures in 2D materials, Adv. Funct. Mater. 2311599 (2024).

[24] R. He, H. Wu, Y. Lu, and Z. Zhong, Origin of negative thermal expansion and pressure-induced amorphization in zirconium tungstate from a machine-learning potential, Phys. Rev. B **106**, 174101 (2022).

[25] S. Plimpton, Fast parallel algorithms for short-range molecular dynamics, J. Comput. Phys. **117**, 1 (1995).

[26] M. Parrinello and A. Rahman, Polymorphic transitions in single crystals: A new molecular dynamics method, J. Appl. Phys. **52**, 7182 (1981).

[27] S. Nosé, A unified formulation of the constant temperature molecular dynamics methods, J. Chem. Phys. **81**, 511 (1984).

[28] R. He, H. Wu, L. Zhang, X. Wang, F. Fu, S. Liu, and Z. Zhong, Structural phase transitions in $SrTiO_3$ from deep potential molecular dynamics, Phys. Rev. B **105**, 064104 (2022).

[29] L. Zhang, M. Chen, X. Wu, H. Wang, W. E, and R. Car, Deep neural network for the dielectric response of insulators, Phys. Rev. B **102**, 041121(R) (2020).

[30] L. Zhang, H. Wang, M. C. Muniz, A. Z. Panagiotopoulos, R. Car, and W. E, A deep potential model with long-range electrostatic interactions, J. Chem. Phys. **156**, 124107 (2022).

[31] W. Dmowski, S. B. Vakhrushev, I. K. Jeong, M. P. Hehlen, F. Trouw, and T. Egami, Local lattice dynamics and the origin of the relaxor ferroelectric behavior, Phys. Rev. Lett. **100**, 137602 (2008).

[32] H. Takenaka, I. Grinberg, and A. M. Rappe, Anisotropic local correlations and dynamics in a relaxor ferroelectric, Phys. Rev. Lett. **110**, 147602 (2013).

[33] K. A. Acosta, H. C. Walker, and A. M. Fry-Petit, Optimizing the dynamic pair distribution function method for inelastic neutron spectrometry, Nat. Rev. Phys. **5**, 236 (2023).

[34] A. Pramanick, W. Dmowski, T. Egami, A. S. Budisuharto, F. Weyland, N. Novak, A. D. Christianson, J. M. Borreguero, D. L. Abernathy, and M. R. V. Jørgensen, Stabilization of polar nanoregions in Pb-free ferroelectrics, Phys. Rev. Lett. **120**, 207603 (2018).

[35] J. Wu, L. Bai, J. Huang, L. Ma, J. Liu, and S. Liu, Accurate force field of two-dimensional ferroelectrics from deep learning, Phys. Rev. B **104**, 174107 (2021).

[36] See Supplemental Material at http://link.aps.org/supplemental/10.1103/PhysRevB.109.054117 for Figs. S1–S8.

[37] Q.-J. Li, H. Sheng, and E. Ma, Strengthening in multi-principal element alloys with local-chemical-order roughened dislocation pathways, Nat. Commun. **10**, 3563 (2019).

[38] S. Chen, Z. H. Aitken, S. Pattamatta, Z. Wu, Z. G. Yu, D. J. Srolovitz, P. K. Liaw, and Y.-W. Zhang, Simultaneously enhancing the ultimate strength and ductility of high-entropy alloys via short-range ordering, Nat. Commun. **12**, 4953 (2021).

[39] V. Fridkin and S. Ducharme, *Ferroelectricity at the Nanoscale: Basics and Applications* (Springer, Berlin, Heidelberg, 2014), p. 1.

[40] A. A. Bokov and Z. G. Ye, Dielectric relaxation in relaxor ferroelectrics, J. Adv. Dielectr. **02**, 1241010 (2012).

[41] A. S. George, The relaxational properties of compositionally disordered ABO_3 perovskites, J. Phys.: Condens. Matter **15**, R367 (2003).

[42] T. Xu, X. Wang, J. Mai, J. Zhang, J. Wang, and T.-Y. Zhang, Strain engineering for 2D ferroelectricity in lead chalcogenides, Adv. Electron. Mater. **6**, 1900932 (2020).

[43] H. Zong, H. Wu, X. Tao, D. Xue, J. Sun, S. J. Pennycook, T. Min, Z. Zhang, and X. Ding, Percolated strain networks and universal scaling properties of strain glasses, Phys. Rev. Lett. **123**, 015701 (2019).

[44] D. Stauffer and A. Aharony, *Introduction to Percolation Theory* (Taylor & Francis, London, 1994).

[45] S. Prosandeev, D. Wang, A. R. Akbarzadeh, B. Dkhil, and L. Bellaiche, Field-induced percolation of polar nanoregions in relaxor ferroelectrics, Phys. Rev. Lett. **110**, 207601 (2013).

[46] I. K. Jeong, T. W. Darling, J. K. Lee, T. Proffen, R. H. Heffner, J. S. Park, K. S. Hong, W. Dmowski, and T. Egami, Direct observation of the formation of polar nanoregions in $Pb(Mg_{1/3}Nb_{2/3})O_3$ using neutron pair distribution function analysis, Phys. Rev. Lett. **94**, 147602 (2005).

[47] J. Parravicini, E. DelRe, S. Perego, M. Acciarri, S. Binetti, Y. Garcia, G. Parapelitsa, A. J. Agranat, and G. Parravicini, Key role of polar nanoregions in the cubic-to-tetragonal phase transition of potassium-based perovskites, Phys. Rev. B **106**, 064107 (2022).